Epitaxial ferroelectric $Hf_{0.5}Zr_{0.5}O_2$ with metallic pyrochlore oxide electrodes

Z. Zhang[1]†, S.-L. Hsu[2,12]†, V. Stoica[3]†, H. Paik[4,5], , E.Parsonnet[6], A. Qualls[6], J. Wang[7], L. Xie[1], M. Kumari[1], S. Das[1], Z. Leng[1]M. McBriarty[8], R. Proksch[9], A. Gruverman[10], D. G. Schlom[4,5,11], L.Q. Chen[7], S. Salahuddin[12], L. W. Martin[1,13], R. Ramesh[1,6, 12]*

[1] Department of Materials Science and Engineering, University of California, Berkeley, California 94720, USA.

[2] National Center for Electron Microscopy, Molecular Foundry, Lawrence Berkeley National Laboratory, Berkeley, California 94720, USA.

[3] Advanced Photon Source, Argonne National Laboratory, Lemont, IL 60439, USA.

[4] Platform for the Accelerated Realization, Analysis, & Discovery of Interface Materials (PARADIM), Cornell University, Ithaca, New York 14853, USA.

[5] Department of Materials Science and Engineering, Cornell University, Ithaca, New York 14853, USA.

[6] Department of Physics, University of California, Berkeley, California 94720, USA.

[7] Department of Materials Science and Engineering, Penn State University, University Park, Pennsylvania 16802, USA.

[8] EMD Performance Materials, San Jose, CA 95134.

[9] Asylum Research, Goleta, CA 93117.

[10] Department of Physics, University of Nebraska, Lincoln, NE 68588-0299.

[11] Kavli Institute at Cornell for Nanoscale Science, Ithaca, New York 14853, USA.

[12] Department of Electrical Engineering and Computer Sciences, University of California, Berkeley, California 94720, USA.

[13] Materials Sciences Division, Lawrence Berkeley National Laboratory, Berkeley, California, 94720, USA.

†These authors contributed equally to this work

Email: rramesh@berkeley.edu

ABSTRACT

We report the synthesis of fully epitaxial ferroelectric $Hf_{0.5}Zr_{0.5}O_2$ (HZO) thin films through the use of a conducting pyrochlore oxide electrode that acts as a structural and chemical template. Such pyrochlores, exemplified by $Pb_2Ir_2O_7$ (PIO) and $Bi_2Ru_2O_7$ (BRO), exhibit metallic conductivity with room-temperature resistivity of < 1 mOhm·cm and are closely lattice matched to yttria-stabilized zirconia (YSZ) substrates as well as the HZO layers grown on top of them. Evidence for epitaxy and domain formation is established with X-ray diffraction and scanning transmission electron microscopy which show that the *c* axis of the HZO film is normal to the substrate surface. The emergence of the non-polar-monoclinic phase from the polar-orthorhombic phase is observed when the HZO film thickness is ≥ ~30 nm. Thermodynamic analyses reveal the role of epitaxial strain and surface energy in stabilizing the polar phase as well as its coexistence with the non-polar-monoclinic phase as a function of film thickness.

INTRODUCTION

Hafnia-based ferroelectrics have attracted tremendous attention due to their robust ferroelectricity at the nanoscale thickness and compatibility with silicon-based microelectronics, making them promising candidates for nonvolatile memory and logic[1-4]. Since their discovery in 2011[5], a worldwide research activity has been aimed at understanding the ferroelectric properties and their translation into applications. From a materials perspective, there has been significant research on the role of chemical substitutions and film thickness, particularly in polycrystalline films deposited by atomic-layer deposition (ALD). It is intriguing to note that many studies have focused on the role of the mechanical constraints imposed by the polycrystalline structure as well as the bottom/top electrodes (typically TiN)[6]. The fact that the polar-orthorhombic phase (O-phase) is a metastable phase (with the non-polar-monoclinic phase (M-phase) being the equilibrium structure)[7], means that single crystals or bulk ceramics are not available to understand the fundamentals of the polar order and pathways by which it can be switched.

Although multiple groups have studied hafnia since its polar phase (space group $Pca2_1$) was first discovered in 2011[5], the formation mechanism of the polar phase in thin films and the switching pathway are still under debate[4, 8] . In the bulk, the polymorph of HfO_2 (and ZrO_2) that is stable at room temperature is the non-polar phase with the monoclinic space group, $P2_1/c$. Other common high-temperature and -pressure polymorphs have tetragonal ($P4_2/nmc$) or cubic ($Fm\bar{3}m$) symmetry[9]. Theoretical calculations show that the O-phase[10] is stable under hydrostatic pressure (3-4 GPa) and has been stabilized via doping[11] and strain[6]. An aspect of interest is the nature of the interfaces between the polar/non-polar phases, which will tell us about the nature of the phase transition from the O-phase to the M-phase. In this regard, Grimley *et al.* [12] have studied the atomic structure of complex mixture of polar domains, non-polar domains, and interface

boundaries in Gd-HfO_2 using high resolution electron microscopy. Park *et al.* [13] revealed the formation of polar phase and non-polar phase with different strain effects using different electrodes. Within the (Hf, Zr)O_2 (HZO) system, $Hf_{0.5}Zr_{0.5}O_2$ has the largest remnant polarization[14]; this is the composition we chose for our studies.

In previous studies on HZO, most samples were grown by ALD and were (111)-textured polycrystalline films[6]. Although the grain boundaries are thought to assist in the stabilization of the metastable O-phase, polycrystalline samples do not provide a simple model system to reveal the intrinsic material properties. In this context, there have been attempts to create epitaxial films of the desired O-phase [2, 3, 15-19]. For example, Wei *et al.*[3] demonstrated the growth of epitaxial (111)-oriented polar HZO films using a (110)-oriented $La_{1-x}Sr_xMnO_3$ layer as the bottom electrode to seed the growth of the HZO layer. Also, epitaxial growth of orthorhombic HZO on (001) Si, (111) Si, and (001) yttria-stabilized zirconia (YSZ) substrates has been demonstrated[15, 17-19]. With this as the background, we set out to study pathways to stabilize the polar O-phase, its stability as a function of thickness, and most importantly how the polarization switching evolves as a function of film thickness.

Recognizing that improved epitaxial growth (*i.e.*, full in-plane orientational locking) of the HZO layer requires seeding it with a bottom electrode that presents a suitable structural and chemical template, we first sought out conducting oxide electrodes that would provide an ideal structural and chemical template to seed the growth of epitaxial HZO layers. Within the large number of conducting oxides[20], we have identified that the family of conducting oxide pyrochlores, exemplified by (PIO) and (BRO) (both with $Fd\bar{3}m$ symmetry and lattice parameters of 10.28 Å and 10.30 Å, respectively)[21, 22], are ideal metallic bottom electrodes for the synthesis of epitaxial HZO layers. A key to our selection of such pyrochlores as the bottom electrode lies in

the fact that the crystal chemistry of pyrochlores bears similarity to that of the HZO system; the formal unit cell of the pyrochlores contains 8 fundamental building blocks and thus there is an approximately 2:1 matching of the unit cell of the pyrochlores with that of HZO. Such pyrochlore iridates and ruthenates also exhibit excellent metallic conductivity with typical room-temperature resistivity $< 10^{-3}\Omega \cdot \mathrm{cm}$[21, 22] are also of interest for electrocatalysis[23] [24]. The presence of two heavy element cations (Pb^{+2} and Ir^{+4}) provides an opportunity for studying the effects of the large inherent spin-orbit coupling on the electronic structure[25]. Finally, it is noteworthy that pyrochlore bismuth ruthenate is extensively used as a contact electrode in multilayer capacitors[26, 27].

The metallic pyrochlore layers are grown on (001)-oriented YSZ substrates. YSZ has a cubic-fluorite structure and its in-plane lattice constant is 5.12 Å. Thus, there is a ~2:1 mapping of the crystallographic dimensions of the YSZ to the pyrochlore. Similarly, there is a ~1:2 mapping of the crystallographic dimensions of the pyrochlore electrode to the HZO phase, as illustrated schematically in **Figure 1(a).** In this orientation, the pyrochlore layer forms an ideal structural and chemical template to seed the growth of [001] oriented layers in the HZO. For HZO, the different phases share similar lattice parameters (Table I)[28]. With this as the basis, epitaxial heterostructures were synthesized using pulsed-laser deposition **(Methods section)**. We have also studied a related pyrochlore electrode, BRO, grown by molecular-beam epitaxy and the results are essentially the same since the crystal chemistry and lattice parameters are very similar to PIO. In order to study the role of epitaxial constraint on phase evolution, we have used the film thickness as the main tuning parameter[29, 30].

RESULTS

X-ray diffraction Bragg scans from films where the HZO thickness varies from 5-50 nm (**Figure 1b,c**) reveal a few important features. First, only 00*l*-type diffraction conditions are observed for both the electrode and HZO layers, with the latter exhibiting an out-of-plane lattice parameter of ~5.05 Å. If we only consider the phase formation from lattice mismatch minimization, the orthorhombic phase ($a, b,$ and $c = 5.23, 5.03,$ and 5.05 Å in bulk) will tend to have its *b* or *c* axis oriented along the surface normal direction with an anisotropic strain from the substrate (2.1% compressive strain on a axis, 1.79% or 1.39% tensile strain on b or c axis); thus the out-of-plane *c* or *b* lattice parameter will expand by 0.1% and 0.3% to 5.055 Å and 5.045 Å, respectively, if the Poisson's ratio is taken to be 0.3[31]. This assumption is validated by the X-ray diffraction data that yields an out-of-plane lattice parameter of 5.05 Å (**Figure 1b,c**). Similarly, if the bulk monoclinic phase ($a, b,$ and $c = 5.11, 5.18,$ and 5.28 Å; $\beta = 100.09°$) were to form, it will tend to have its orthogonal *a* and *b* axes oriented in the plane of the film with only a uniaxial 1.16% compressive strain. We did not, however, distinctly observe the corresponding peak (which should appear at ~34.3°) in the X-ray diffraction patterns. That suggests the monoclinic phase is unlikely to be formed as the dominant phase in the orientation described above. However, given the similarity in the structure of the O-phase and the M-phase (with small differences in oxygen and Hf/Zr positions), the presence or absence of either phase cannot be uniquely identified by just Bragg scans, particularly for HZO film thicknesses of ~ 5nm.

We performed hard X-ray reciprocal space mapping (RSM) for the 15 nm, 30 nm and 40 nm HZO samples (**Figure1d,e,f**) using the higher beam intensity and resolution available in a synchrotron facility (details in Methods section). RSM's were obtained about several zone axes to obtain converging structural information. For the sake of simplicity, we present the main conclusions in **Figure 1(d,e,f)** and the full details are presented in Supplemental **Figure S4,5,6**.

The RSM data for the 15 nm sample around its 224 peak demonstrates that the film is coherently strained by the substrate and the bottom electrode; the diffraction peak of the HZO layer is confirmed from the O-phase, with nanodomains oriented in multiple directions. In contrast, in the case of the 40 nm sample, the RSM shows that the HZO peak is separated from the PIO and YSZ peaks. More importantly, the intensity of the O-phase peak has decreased; instead, the M-phase becomes the dominant phase. The multiple, split-peaks corresponding to the M-phase indicate that it exists in multiple orientations in the 40 nm sample; this is validated by direct electron microscopy studies of cross-section samples (**Figure 2**). The RSM of the 30 nm sample shows the transitional state in between, where the M-phase shows up but only has a vague range in reciprocal space. Thus, increasing the film thickness progressively leads to the destabilization of the O-phase with a concomitant stabilization of the M-phase.

Atomic resolution dark field and bright field scanning transmission electron microscopy (STEM) images indeed confirm that the model structure of the tri-layer structure, shown schematically in **Figure 2a**, is indeed valid, illustrating the in-plane lattice matching between the PIO and HZO with a ~1:2 ratio. To understand the microscopic details of the phase stability in the HZO layer as a function of thickness[32], we carried out high-angle annular dark-field scanning transmission electron microscopy (HAADF-STEM) and bright-field STEM (BF-STEM) imaging in conjunction with detailed atomic-scale simulations for the PIO/HZO/PIO and SRO/HZO/PIO heterostructures with 5- and 30-nm-thick HZO layers. For an HZO film thickness of 5 nm (**Figure 2b**), HAADF-STEM imaging reveals the epitaxy of the HZO layer sandwiched by the top and bottom PIO layers with sharp interfaces and demonstrates that the cation sublattice is fully epitaxial on top of the PIO layer. Nevertheless, unique identification of the crystal phase using only the cation sublattice can lead to ambiguity since there are other crystal structures that show a

similar cation sublattice arrangement (such as the non-polar-orthorhombic *Pbcm* and monoclinic $P2_1/c$ phases, as illustrated in **Figure S1**). For example, although the monoclinic $P2_1/c$ phase has a different cation sublattice arrangement when compared to the orthorhombic $Pca2_1$ phase, the main difference within the similar cation sublattice arrangement between $Pca2_1$ and *Pbcm* phases is the oxygen ratio and location (as illustrated in **Figure S1a-i,** and **Figure S1j-r)**. Here, heavy atoms such as hafnium, zirconium, lead, and iridium can be easily imaged by HAADF-STEM, in contrast to light atoms such as oxygen, due to the Z-contrast sensitivity.

Therefore, to distinguish the non-centrosymmetric phase from other structurally similar centrosymmetric phases, BF-STEM imaging, in conjunction with image simulations, was employed to further resolve the oxygen anion positions and thus identify the symmetry accurately. As shown in **Figure 2b** (right), the oxygen sublattice of HZO demonstrates two regions (O- [001] and O- [010]) of the polar $Pca2_1$ phase and double oxygens in O- [001] and zig-zag oxygen arrays in O- [010] do not match with the non-polar *Pbcm* phase (**Figure S1s**). The image contrast for the hafnium/zirconium and oxygen sublattices are in good agreement with the atomic model of the ferroelectric $Pca2_1$ phase, validated with image simulations (**Figure S2**). Besides, the experimental results do not match with the simulated image of the monoclinic $P2_1/c$ phase, because only M-[001] shows similar hafnium/zirconium sublattices with *Pbcm* and $Pca2_1$ phases. However, subtle differences such as a smaller spacing of zig-zag oxygen dumbbells and single oxygen of zig-zag array can be observed (**Figure S1d-h**).

For the 30nm HZO film (**Figure 2c**), the HAADF-STEM image reveals that the hafnium/zirconium sublattices maintains the same orthorhombic structure as the 5-nm-thick HZO films. A minor fraction of the monoclinic $P2_1/c$ phase was also identified, and it coexists with the orthorhombic $Pca2_1$ phase in films of such thickness(**Figure S3c**) ; indeed, this appears to be very

close to a critical thickness for the transition from the O-phase to the M-phase. The BF-STEM images reveal that the hafnium and oxygen sublattices are matched with the *Pca*2_1 phase atomic model. Importantly, STEM simulations (**Figure 2d**) using the Prismatic code [33] [34]compute the exact positions of hafnium and oxygen ions for the *Pca*2_1 phase along the [100] zone axis under BF-STEM experimental conditions. The result matches closely with the HAADF and BF-STEM images. Perhaps the most interesting aspect to films of such thickness is the appearance of "finger-like" features near the electrode-HZO interface, which appears to be an indicator of the impending structural phase transition for thickness higher than ~30nm.

With a further increase in thickness to ~50 nm, the top portion of the HZO layer clearly shows the formation of "finger-like" features; these "finger-like" features can be identified as the monoclinic phase, which is now the dominant phase, identified through the atomic resolution images in **Figure 2e,** and elaborated in **Figure S3a, b**. Hence, the ferroelectric *Pca*2_1 phase, that can be stabilized through epitaxy, progressively converts into the monoclinic phase as the HZO layer thickness is increased.

Probing the ferroelectric phase

When probing the polar order in ultra-thin films such as those being studied in this study, it is critical to ensure that the effects of leakage are accounted for and eliminated. Therefore, we used a combination of voltage-dependent piezoelectric susceptibility measurements in a capacitor geometry (which should be less susceptible to leakage effects) coupled with piezoresponse force microscopy (PFM) of the exposed HZO followed by conventional polarization-voltage measurements. Portions of the exposed HZO surface were poled with opposite polarity voltages

and imaged using PFM, an example of which is shown (**Figure 3a, b**) for a 10-nm-thick HZO film. The amplitude image (**Figure 3a**) shows a strong piezoelectric response, while the corresponding phase image (**Figure 3b**) shows a 180**°** change in the phase of the output signal, indicating that the polarization state has been switched by a corresponding angle by the opposite polarity voltage. These PFM images are stable for well over 24 hours, indicating the ferroelectric origin of the image contrast.

In order to probe the switching behavior quantitatively, we applied a DC voltage to 12.5-μm-diameter, 30 nm $SrRuO_3$ (SRO) / 5, 10, 15, and 30 nm HZO / 20 nm PIO capacitors in the PFM and obtained piezoelectric phase/amplitude versus DC field loops for samples with different thicknesses. (For ease of fabrication for the top electrodes via wet etching, we used a top electrode of SRO that was grown *in situ* and processed into circular capacitors (**Methods**)). Piezoelectric hysteresis loops (both phase and amplitude as a function of applied DC voltage) were obtained both for the capacitor geometry as well as for the bi-layer structure (i.e., no top electrode). The piezoelectric response [35]was measured using a standard test protocol (**Methods**) in which an *ac*-voltage signal is fed onto the cantilever and induces a piezoelectric response from the ferroelectric surface which is then picked up using a lock-in technique. A square wave DC bias was applied with pulse width varying from 0.01s to 1s that steps up/down in magnitude with time (schematically illustrated in **Figure 3c**). It is noteworthy that the effective frequency of this triangular shaped pulse profile is of the order of a few Hz, as illustrated in Figure 3b. Piezoelectric responses were measured both at the top of the DC pulse (ON-state) as well as at the bottom of the DC pulse (OFF-state).

Figure 3d&e summarize the piezoelectric phase vs. DC field plots for films of varying thickness in both ON- and OFF-field modes. We do observe a decrease in the coercive field as the

HZO thickness increases, which is generally consistent with the expected dependence of E_C on thickness (d)[36] [37]; however, since the thickness range is quite limited, we are able to draw only qualitative conclusions about such scaling. However, an intriguing observation is the marked difference in coercive field between the ON-state and OFF-state measurements. The coercive field in the OFF-state measurement is still much higher (~1 MV/cm) than what is well-known for perovskite based ferroelectrics[38], and is consistent with prior reports for HZO[3]. However, the coercive field in the ON-state measurement is ~3-5 times smaller for the same capacitor; specifically, for the 30nm thick film, it shows an ON-state coercive field of about 200kV/cm. For the sake of completeness, supplementary **Figure S7** presents the amplitude and the phase responses for the 5nm thick sample.

To explore this rather puzzling and surprising result, we first went back to well-known ferroelectrics such as $BiFeO_3$ and the lead zirconate titanate (PZT) family. We carried out the same set of measurements described above for the HZO films for $BiFeO_3$ with $SrRuO_3$ top and bottom electrodes with a thick (100 nm) and a thin (6 nm) BFO layer respectively. The results of this measurement are shown in supplemental **Figure S8**. It is apparent that in the thick sample, the ON-state and OFF-state data are essentially the same, i.e., the switching voltage extracted from either piezoelectric phase loop (ON and OFF) is ~2V; indeed we have been able to obtain such data repeatably for thick (typically greater than ~20nm) layers of other commonly studied ferroelectrics (such as $Pb(Zr, Ti)O_3$, $BaTiO_3$, $La\text{-}BiFeO_3$). On the other hand, in the thin (~6nm) BFO sample, the ON and OFF data show a significant difference in the switching behavior characterized by a switching voltage that is measurably smaller in the ON state versus the OFF state; we have observed essentially the same trend in PZT thin films. Finally, to remove doubts about this being an artefact of the measurement system, we measured the same sample using the

Asylum Cypher system equipped with an interferometric detection system (IDS) at the Asylum test facility, the results of which are presented in **Figure S9;** they show the same difference in the switching field between the ON and OFF states. We note that such a distinct difference in the piezoelectric switching in the ON vs. OFF state has not been reported in the PFM based switching studies literature[39-41].

Based on our observations, we believe that a full, detailed study of the switching dynamics of ultrathin ferroelectrics is warranted; however, that is not the central focus of this paper, although it is certainly a key outcome of our attempts to address the switching field of HZO-based ferroelectrics. So: why the difference between ON and OFF PFM responses? Our hypothesis is that in ultrathin films (such as the HZO films in this study as well as the very thin BFO that we have used as reference), the existence of a strong depoling field[42, 43] drives a rapid polarization relaxation after the voltage pulse is removed. Under this scenario, a fraction of dipoles flip back opposite the poling direction effectively instantaneously once the field is removed; thus, in order to get to achieve the remnant state in the OFF field, a higher coercivity is observed.

To probe the remnant polarization (P_r) we carried out polarization (P)-electric field (E) hysteresis loop and pulsed polarization measurements on the same set of capacitors (**Figure S10a-e**). As we expected, measurements below a thickness of 7.5 nm were compounded with leakage due to the macroscopic size of the capacitors; for the same reason, polarization hysteresis loops were measured at 100kHz to minimize resistive leakage. The remnant polarization of the 7.5-nm-thick film reaches a value of ~30 $\mu C/cm^2$. The theoretical P_r of the (001)-oriented orthorhombic phase of hafnia could be as large as 51-53 $\mu C/cm^2$.[6] For a 30 nm HZO film, we observe a measurable ferroelectric state (consistent with the TEM studies) with a $P_r \approx 10\ \mu C/cm^2$. Beyond this thickness, we observe a progressive conversion into the M-phase, again consistent with the

STEM observations, **Figure 2(e).** This result can be put into context with published results for HZO on commonly used electrodes; for example, P_r was nearly zero for TiN/HZO/TiN thicker than ~20-25 nm.[14, 29] The coercive voltage measured at this frequency of 100kHz is higher than what is observed in the piezoelectric phase loops for the same capacitor (**Figure 3d, e**), illustrating the frequency dispersion in the switching voltage. The polarization switching response was measured under pulsed probing conditions, which is schematically illustrated in **Figure S10b**. A preset pulse polarizes the material into a uniform polarization state, whereafter two sequential, identical probe pulses, first switch the polarization and then measure directly the non-switching (dielectric) response of the material. We are able to thus determine the displacement current contribution from polarization switching alone by subtracting the non-switching response from the switching response. This so-called switching current transient is illustrated in **Figure S10c**. Upon integrating this switching current transient, one obtains the switched polarization as a function of time, for two different nominal voltages of 8V and 4.8V, and for both positive and negative polarities. These pulsed switching studies show a robust switched polarization for films up to 30nm in thickness.

To understand why the polar-orthorhombic phase is stable in our epitaxial samples, we analyzed the phase stability and coexistence of the non-polar-monoclinic and polar-orthorhombic phases of HZO using a simple thermodynamic model. Three energy contributions were considered towards the total Gibbs free energy: the Helmholtz free energy $U - TS$ (where U is the enthalpy, T is the absolute temperature, and S is the entropy), the surface energy (γ), and the elastic-strain energy ($\frac{1}{2}\sum_i \sigma_i \varepsilon_i$) as:

$$G = U - TS + \mathrm{A}\,\gamma + \frac{1}{2}V \cdot \sum_i \sigma_i \varepsilon_i \qquad (1)$$

The thermodynamic terms, surface energy, and the lattice parameters of the polar-orthorhombic and non-polar-monoclinic phases were obtained from published values (**Supplementary section**). Since there is a diversity of such values, we considered all possible combinations of lattice parameters and surface energies, which give rise to the free-energy bands for the monoclinic and orthorhombic phases. **Figure 4a** shows the Gibbs free energy per unit volume of the non-polar-monoclinic and polar-orthorhombic phases versus film thickness and gives an intuitive impression of the phase stability as a function of film thickness. The first important conclusion is that the polar-orthorhombic phase is more stable in thinner films since the surface energy of the orthorhombic phase is lower than that of the monoclinic phase. When the film gets thicker, the monoclinic phase gets more stable, primarily as a consequence of the strain-energy contribution increasing and the surface-energy contribution decreasing with film thickness. This is consistent with the experimental data, *i.e.*, thinner samples have pure orthorhombic structure, while the monoclinic phase starts to grow in fraction as the sample gets thicker. In ~50-nm-thick films, we barely observe any orthorhombic phase and what little that is observed is found at the electrode-HZO interface.

Realizing that the film thickness is a key parameter, we further computed the energetics of a coexistence state of the monoclinic and orthorhombic phases as a function of thickness (**Figure 4b**). Both the RSM and STEM data reveal that the strain from the substrate gets relaxed in thicker films. Thus, we considered the strain relaxation because of the dislocations in the calculation of **Figure 4b**. The effective misfit strain as a function of thickness is evaluated using the Matthews-Blakeslee criterion:

$$\varepsilon(h) = 1 - \frac{1 - \varepsilon_0}{1 - \varepsilon_0\left(1 - \frac{h_c}{h}\right)} \qquad (2)$$

where h is the film thickness and h_c is the Matthews–Blakeslee (MB) critical thickness for dislocation formation[30]. These calculations were performed as a function of h_c, the critical thickness, as shown in **Figure 4b**, to estimate the volume fraction of the orthorhombic phase as a function of thickness and to illustrate the effects of strain relaxation on the relative stability of the two phases. When $h_c = 1\ nm$, *i.e.*, the strain was relaxed by dislocation formation at this thickness, the vertical line shows that the orthorhombic phase and monoclinic phase cannot coexist in the sample. The polar orthorhombic phase disappears in thicker samples. On the contrary, in the scenario of $h_c = 100\ nm$, *i.e.*, the film is coherently strained until this thickness, the orthorhombic phase volume fraction asymptotically drops to ~60% at this limit but is still stable. For critical thicknesses in between, the orthorhombic phase volume fraction will drop to zero at a thickness that is directly related to the critical thickness. Relating this to our experimental results, the critical thickness h_c is estimated to be ~25 nm. Increasing the critical thickness by eliminating the dislocations in samples will help the polar orthorhombic exist in thicker films.

Discussion

The work presented in this paper clearly points to the role of epitaxial strain and surface energy in stabilizing the polar O-phase; relaxation of the misfit strain with film thickness emerges as a key element in destabilizing the polar-orthorhombic phase in favor of the non-polar-monoclinic phase. This also points to the possibility of further stabilizing the polar-orthorhombic phase at larger film thicknesses by epitaxial constraint, for example by using a bottom electrode that imposes a smaller lattice mismatch strain (and thus increasing the h_c value). It is equally interesting to note from the STEM images of the thicker HZO layers (*i.e.*, > 30 nm) that the interface between the polar-orthorhombic phase and the non-polar monoclinic phase is rather diffuse (*i.e.*, it does not appear

to be a consequence of a diffusion-less, shear transformation, as, for example, in martensites). Instead, the diffuse nature of this interface indicates a possible order-disorder type of phase transition from the polar-orthorhombic phase to the non-polar-monoclinic phase. Thus, one possible pathway to prevent the formation of the non-polar-monoclinic phase could be the rate of cooling from the deposition temperature to prevent such diffusional processes.

In conclusion, we have demonstrated epitaxial stabilization of the polar orthorhombic HZO phase using a new lattice matched bottom electrode PIO at a film thickness of $\leqslant$ 30 nm. Atomic resolution STEM images for these epitaxial films directly show the phase evolution as a function of film thickness and provide an ideal way to further study the switching pathway and the possible electric-field-induced phase transformation. Thermodynamic calculations reveal the critical role of epitaxial strain and surface energy in stabilizing the orthorhombic phase over the monoclinic phase. Thus, it appears that further tuning of the phase space through such an epitaxial stabilization process could lead to the orthorhombic phase being stable over an even larger thickness range, which may further help in reducing the switching field. Perhaps the most intriguing aspect of our study is the possibility that the switching field (i.e., coercive field) could possibly be much lower than what has been published so far; understanding of the polarization dynamics in detail would be key to unraveling this.

Materials and Methods

Growth

The 30 nm $SrRuO_3/x$ nm $Hf_{0.5}Zr_{0.5}O_2/20$ nm $Pb_2Ir_2O_7$ heterostructure were grown on (001)-oriented, single-crystalline YSZ substrates by pulsed laser deposition using a KrF excimer laser (248 nm, LPX 300, Coherent), where the thickness of HZO varies in the range from 5 to 50 nm ($i.e., x = 5, 7.5, 15, 30, 40, 50$ nm). The growth of all layers was carried out in a dynamic oxygen pressure of 100mTorr, at a growth temperature of 600 ℃, and a laser repetition rate of 2 Hz. The laser fluence for PIO and HZO/SRO are $1.25\ \mathrm{J}/cm^2$ and $1.0\ \mathrm{J}/cm^2$, respectively. Following growth, the samples were cooled to room temperature at a cooling rate of 10 ℃/min under a static oxygen pressure of 1 atm.

Capacitor Fabrication

Circular top electrodes (diameter 12.5 μm) were fabricated using a wet etching method. Due to the ease of a simple wet etch process, for these measurements we used a SrRuO3 (SRO) top electrode. First, the photoresist was patterned on the as-grown heterostructures using photolithography, which only covers the circular electrode regions. The rest region of the top SRO was etched away within 1 min under ~0.02 mol/L $NaIO_4$, leaving circular SRO contacts covered by the photoresist. Subsequently the photoresist was removed by an acetone rinse.

X-ray Measurements

A high-resolution X-ray diffractometer (Panalytical, X'Pert3MRD) was used to perform Bragg line scans. Copper K-alpha radiation was used for the X-ray diffraction measurements. All the XRD curves were calibrated by the substrate peak (5.12 Å, $35.02°$).

The RSM was performed by synchrotron X-ray diffraction. The high flux from a synchrotron source at 33-ID-B and 33-BM-C beamlines of the Advanced Photon Source, Argonne National

Laboratory, was best suited for determining the lattice modulations associated with the nanoscale films. The X-ray energy was 20 keV in combination with Kappa 6-circle diffractometer at the 33-ID-B beamline, while 16 keV and Huber 4-circle diffractometer were used at 33-BM-C beamline. The PILATUS 100K pixel detector was used at both beamlines to obtain 3Dreciprocal space maps (RSMs) with high accuracy and speed. Reconstruction of the XRD data was used to convert into the reciprocal space representation of the data using rsMap3D, while cuts along different directions of reciprocal space were employed to the create different views.

Electron microscopy

The cross-sectional TEM samples of HZO heterostructures were mechanical polished using an Allied High Tech Multiprep at a 0.5° wedge. After thinning the total thickness of samples down to 10 μm, the TEM samples were Ar ion milled using a Gatan Precision Ion Milling System to an electron-transparent sample starting from 4keV down to 200ev as final cleaning energy. The atomic scale HAADF-STEM images of HZO heterostructures were performed by Cs-corrected TEAM1 FEI Titan 80-300 microscope operated at 300kV using a high-angle annular detector for Z-contrast imaging and the beam convergence angle was 17 mrad. The outer detector angle for BF-STEM imaging was ~1 mrad and the inner angle for HAADF imaging was 50 mrad. The experimental images were processed by Wiener filter to reduce noise. STEM image simulations were calculated approximately close to the experimental conditions to identify HZO phases using the Prismatic[33, 34] method, especially the oxygen positions of HZO.

Electrical Characterization

Piezoresponse force microscopy images and piezoresponse loops were measured at room temperature using a scanning probe microscope (Asylum MFP-3D).

The piezoresponse results were proved by the same set of measurements in Asylum, using the IDS (interferometric detection system), with varying driving voltage and pulse width.

Ferroelectric polarization hysteresis loops were measured at room temperature using a Precision Multiferroic Tester (Radiant Technologies). The measurements were completed at a frequency of 100kHz.

Figures and Tables

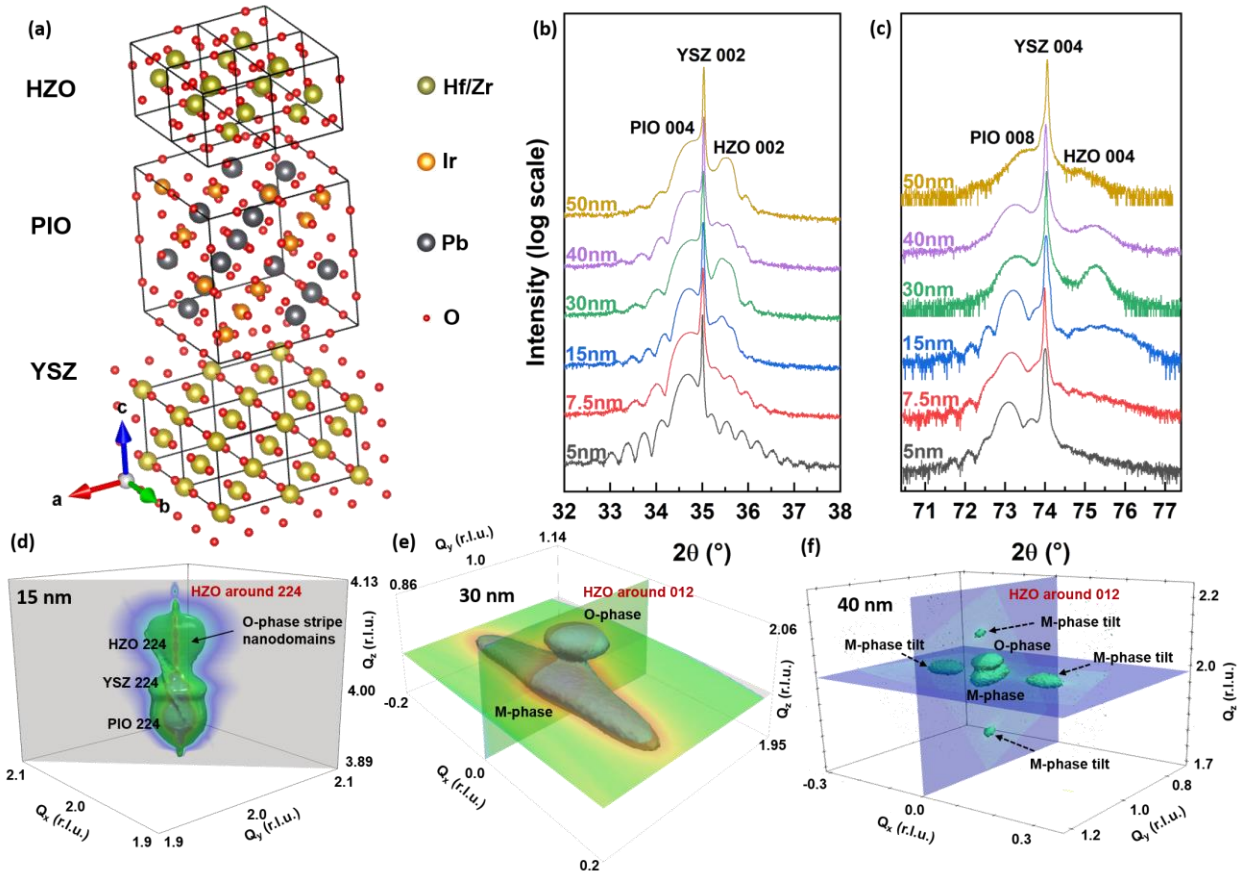

Figure 1. Thickness dependent structural characterization using XRD & RSM. (a) Schematic of the lattice matching between the pyrochlore electrode, the substrate YSZ and the HZO layer; **(b)** X-ray diffraction line scan about the $(002)_{HZO}$ peak for 5-50 nm HZO/ 20 nm PIO heterostructures; **(c)** is the corresponding scan around the $(004)_{HZO}$ peak; **(d)** Hard X-Ray reciprocal space mapping about the $(224)_{YSZ}$ peak for 15 nm HZO on 20 nm PIO; **(e)** Hard X-Ray reciprocal space mapping about the $(012)_{HZO}$ peak for 30 nm HZO on 20 nm PIO; **(f)** Hard X-Ray reciprocal space mapping about the $(012)_{HZO}$ peak for 40 nm HZO on 20 nm PIO.

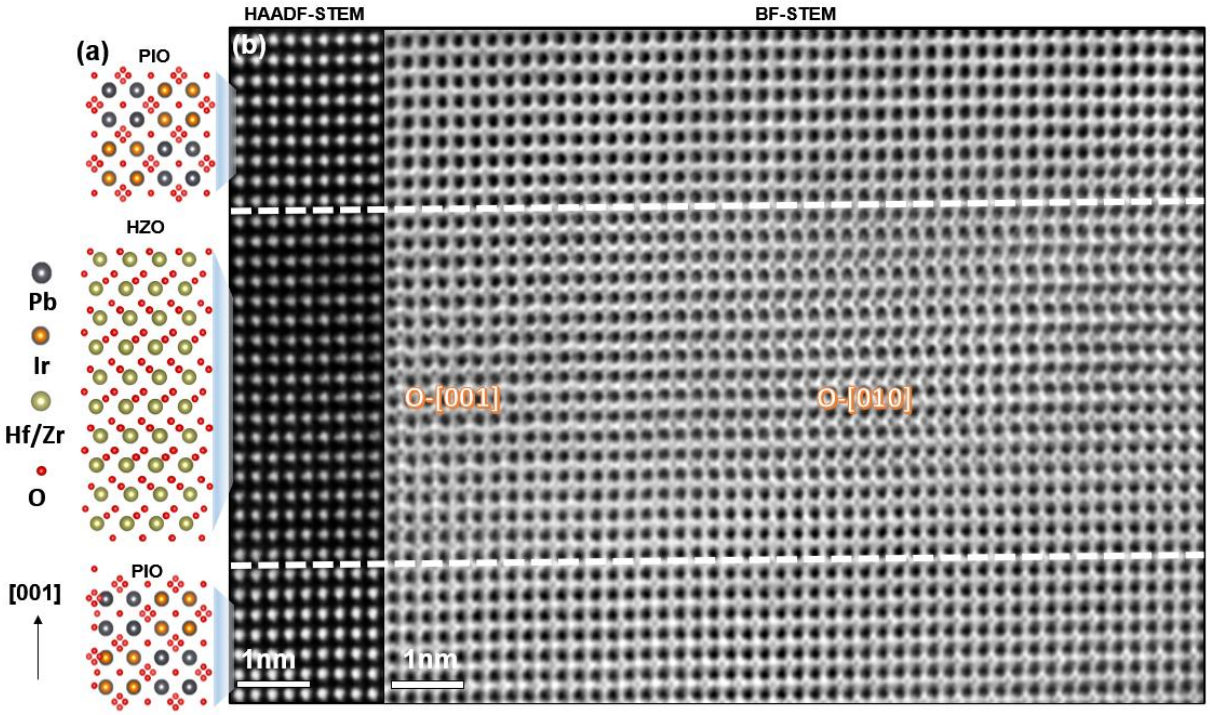
HAADF-STEM
BF-STEM
(a)
PIO
HZO
PIO
Pb
Ir
Hf/Zr
O
[001]
(b)
O-[001]
O-[010]
1nm
1nm

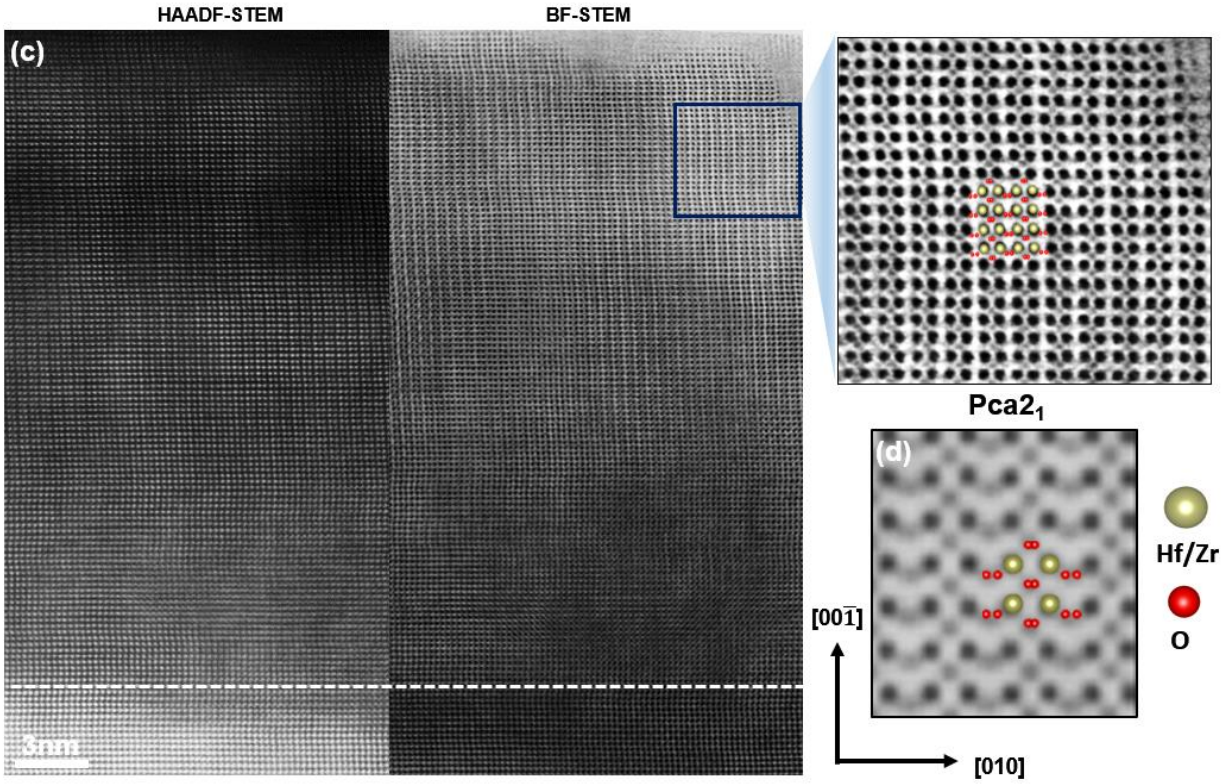
HAADF-STEM
BF-STEM
(c)
5nm
Pca2$_1$
(d)
Hf/Zr
O
[00$\bar{1}$]
[010]

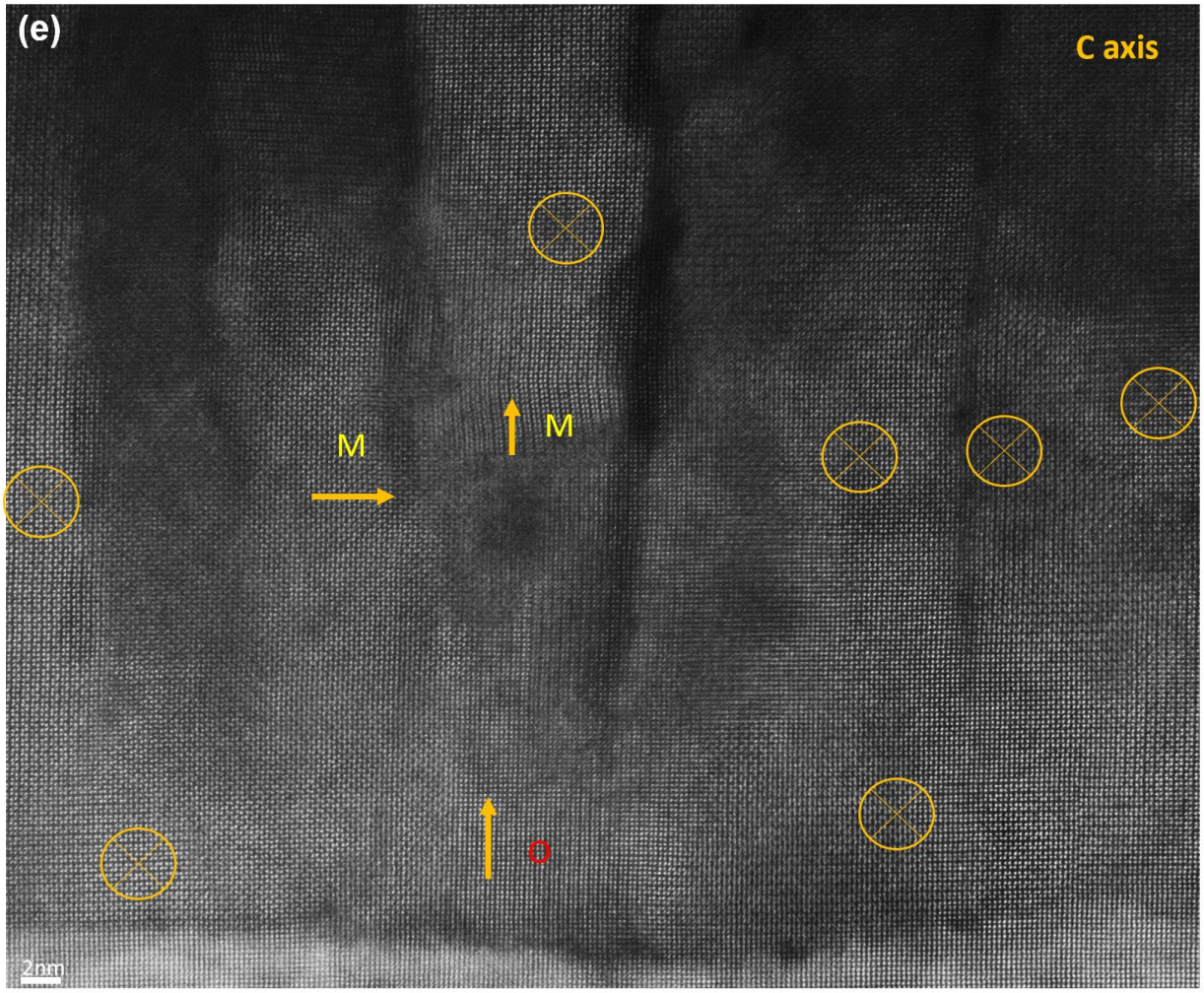

Figure 2. Direct imaging of polar structure using STEM

Schematic of the atomic structure **(a)** of the PIO/HZO/PIO heterostructure. Using HAADF/BF-STEM imaging, ferroelectric phase in **(b)** epitaxial PIO/ HZO(5nm)/ PIO heterostructures and in **(c)** epitaxial SRO/ HZO (30 nm)/ PIO with high magnification of BF-STEM **(d)** Simulated STEM image of orthorhombic phase with space group symmetry of $Pca2_1$. **(e)** A HAADF -STEM image of the 50nm HZO sample showing the formation of monoclinic domains in the "finger" -like top portions of the film, while the regions near the electrode interface start off as the orthorhombic phase. Orange notation refers to the c-axis of HZO.

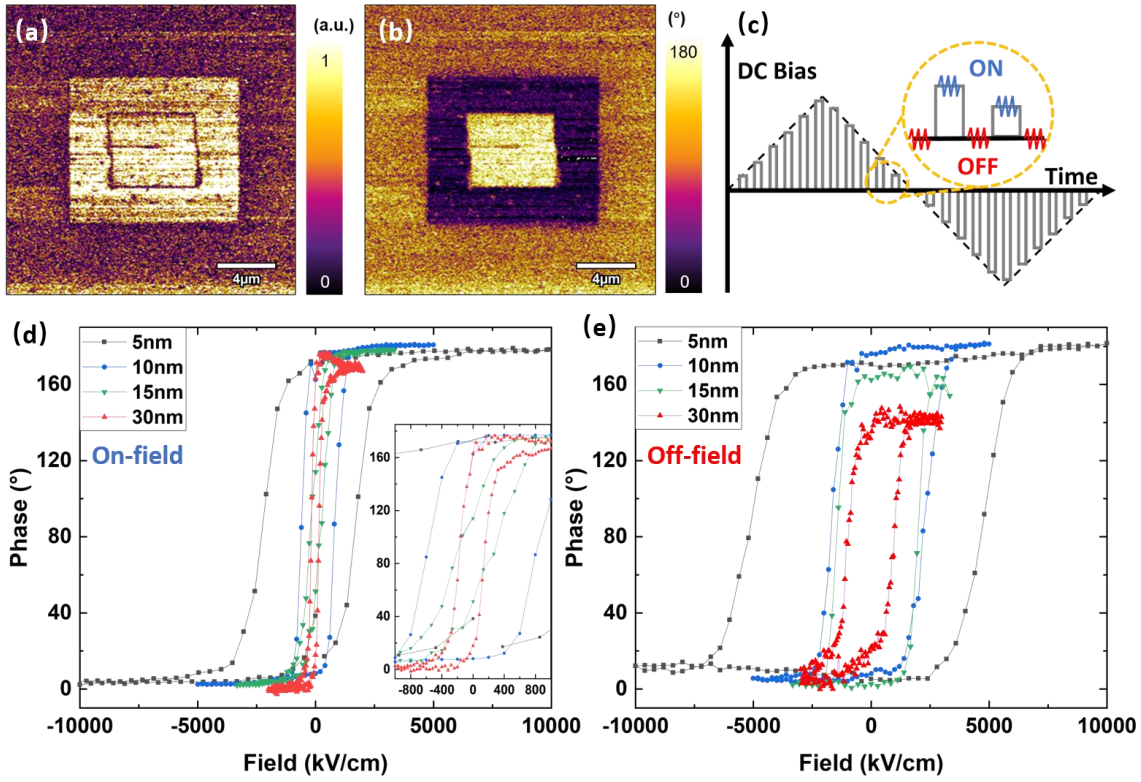

Figure 3. Piezoresponse force microscopy measurements

Piezoresponse force microscopy image written by an AFM tip on 10 nm HZO/ 20 nm PIO heterostructure, **(a)** amplitude signal and **(b)** the corresponding phase signal; Piezoresponse loops measured on 30 nm SRO/ (5,10,15,30) nm HZO/ 20 nm PIO heterostructure capacitors, **(c)** Schematic illustration of the DC pulses and the ON/OFF measuring modes **(d)** measured at the top of DC bias pulse (ON) **(e)** measured at the bottom of the DC bias pulses (OFF).

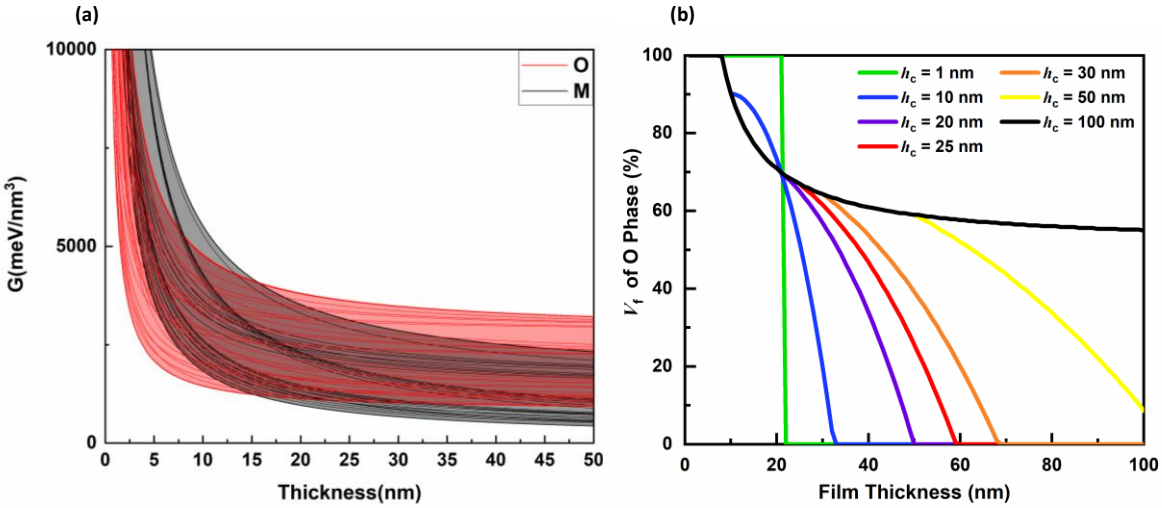

Figure 4. Thermodynamic calculation of thickness dependent stability of m- and polar O-phases

(a) Gibbs free energy bands of *m*- and polar *O-phase* as a function of film thickness at room temperature for an epitaxial HZO films calculated based on all possible parameters from the literature.

(b) Simulation of the volume fraction of the polar *O-phase* as a function of film thickness at room temperature with different strain relaxation critical thicknesses.

Table I. HZO Lattice Constant[28]

	a **(Å)**	***b*** **(Å)**	***c*** **(Å)**
monoclinic phase ($\beta = 100.09°$)	5.11	5.18	5.28
orthorhombic phase	5.23	5.03	5.05

Supplementary Materials

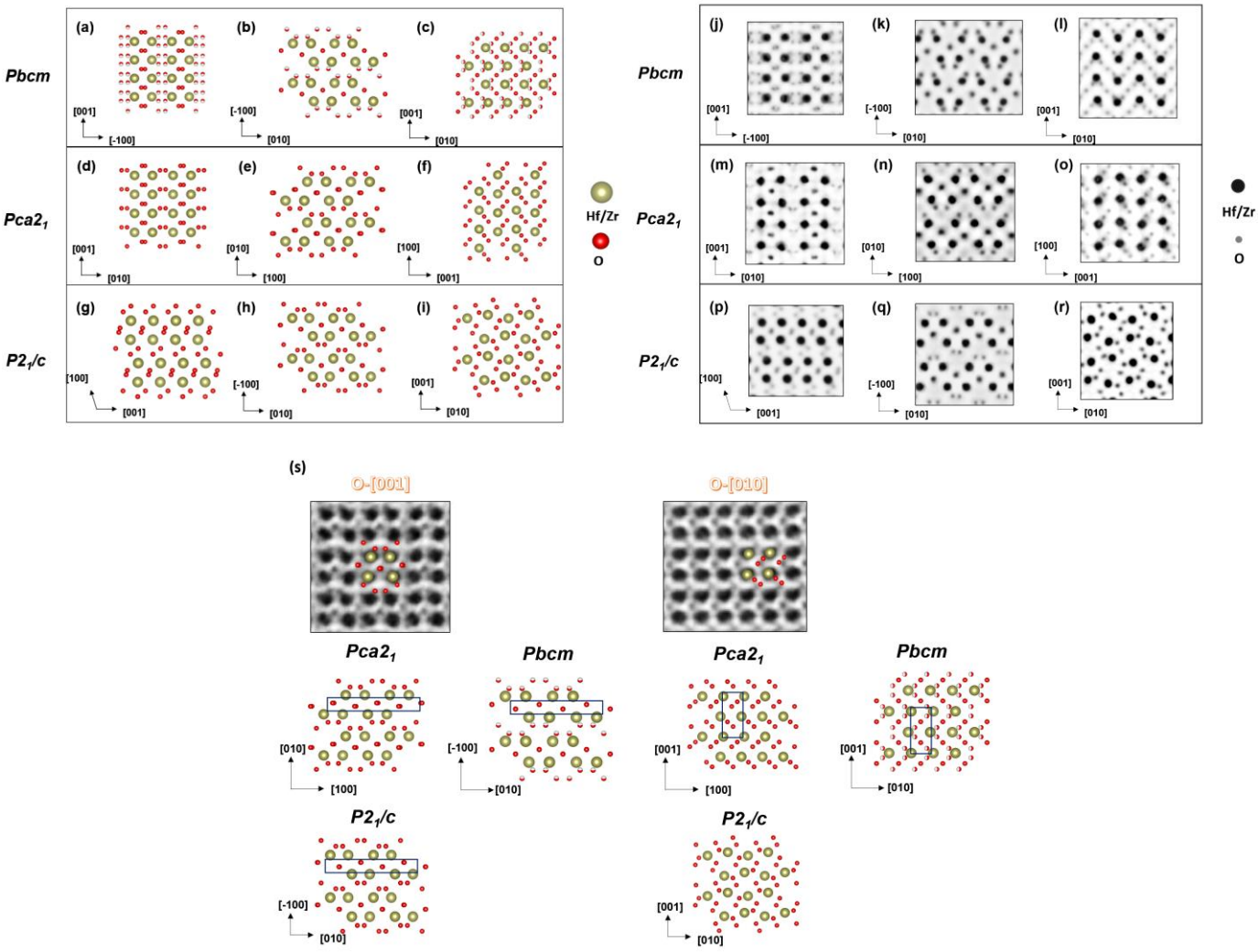

S1. Comparison between the centrosymmetric *Pbcm*, non-centrosymmetric *Pca2₁*, and monoclinic *P2₁/c* phases.

Different orientations of the crystal structure of HZO in *Pbcm*, *Pca2₁*, and *P2₁/c* HZO symmetry **(a)-(i)** corresponding to multislice simulation **(j)-(r)** showing the similar hafnium/zirconium sublattices and the differences of oxygen ratios and locations in **(a)(d)(j)(m), (b)(e)(h)(k)(n)(q),** and **(c)(f)(l)(o).** For example**,** double oxygens of horizontal zig-zag arrays in **(e)** comparing to

single oxygen in **(b)** and distinct oxygen positions in **(a)(d)** and **(c)(f)** can help identify the *Pbcm* or *Pca2₁* phase with their similar hafnium/zirconium sublattices. Phase comparison between *Pca*2$_1$, *Pbcm*, and *P2₁/c* in **(s)** to identify O- [001] and O- [010].

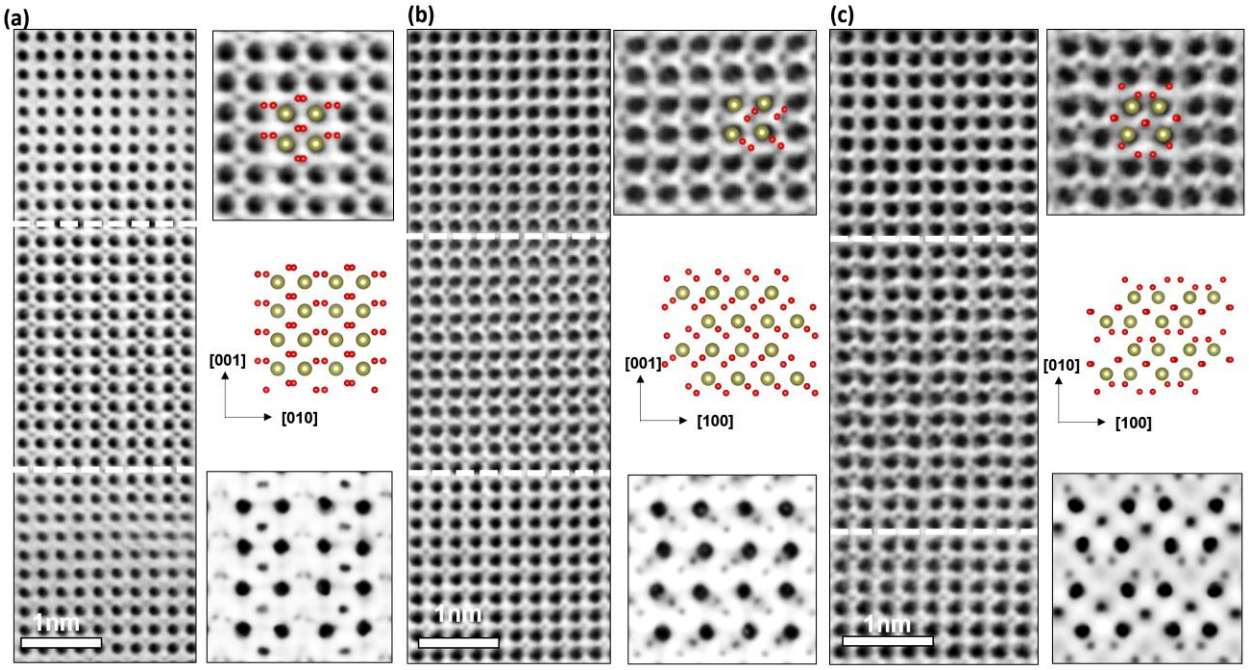

S2. Ferroelectric O-phase with three variants in the 5 nm PIO/HZO/PIO heterostructure

Atomic scale HAADF- STEM imaging of HZO heterostructures demonstrates the co-existence of all three structural variants in the *O-phase* (*Pca*2$_1$ phase) with the electron beam along the **(a)** [100], **(b)** [010], and **(c)** [001] zone axes of the HZO film, respectively. Each zoom-in imaging of (a), (b), and (c) corresponds to their crystal structure and multislice simulation. This shows the formation of nanoscale polar domains in the HZO layer. According to **S1** comparison, these three

zone axes of the HZO film are not $P2_1/c$ phase because hafnium/zirconium sublattices in **S1d,g** and **S1f,i** are totally different and subtle differences in **S1e,h** such as double oxygens of horizontal zig-zag arrays and larger spacing of zig-zag oxygen dumbbells in $Pca2_1$ phase.

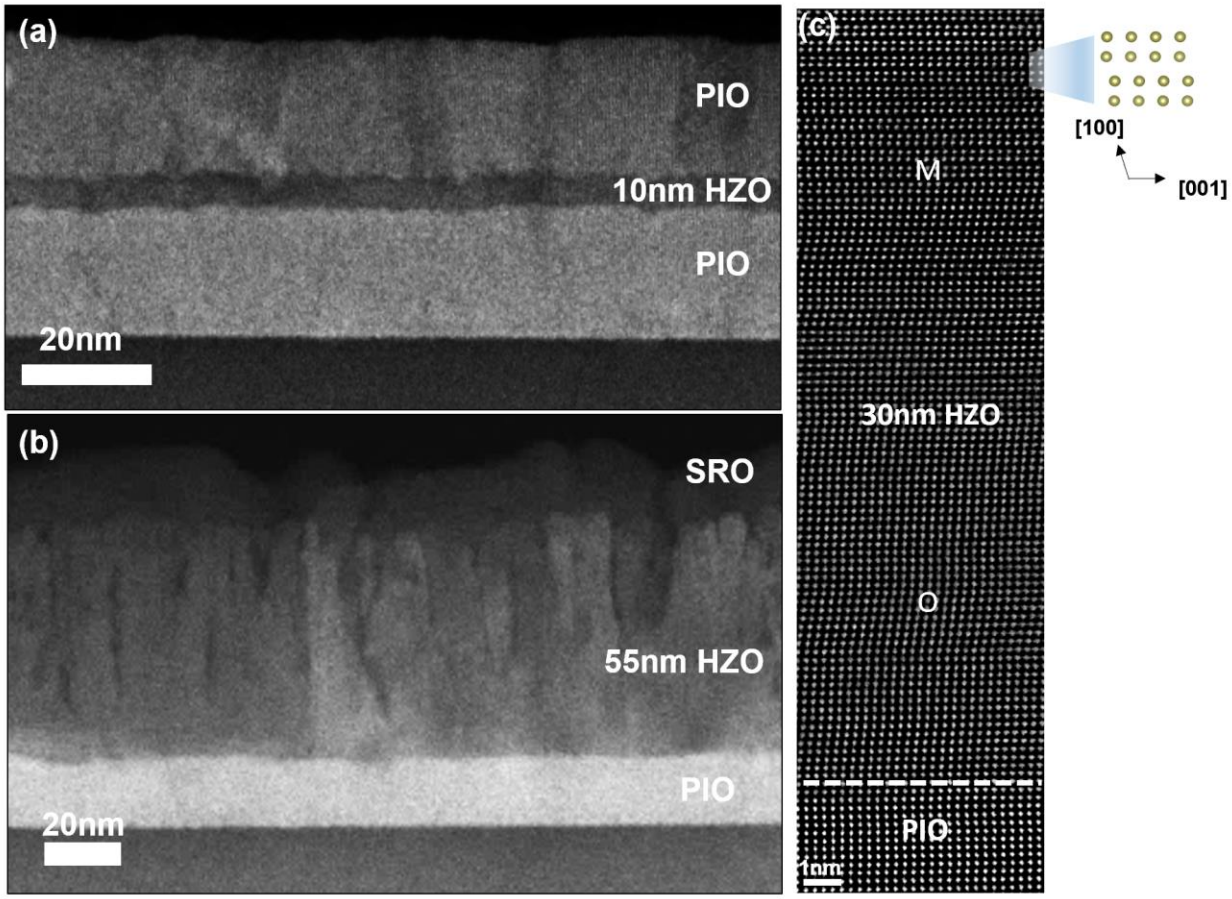

S3. Thickness dependence of HZO morphology and two-phase coexistence in epitaxial HZO heterostructures

Cross-section TEM images of the 10 nm HZO heterostructure compared to that with ~55 nm HZO thickness: **(a)** 10 nm, showing a relatively smooth HZO interface, although the early stages of surface rumpling are already evident in this image; **(b)** 55 nm HZO film, where the "finger-

like" features in the HZO layer is very clear. A monoclinic $P2_1/c$ crystal structure can be identified using the HRSTEM images of the hafnium/zirconium sublattices; **(c)** shows the coexistence of the *O-phase* with the *M-phase*; the *O-phase* is predominantly observed at the electrode-HZO interface, suggesting that the initial stages of nucleation occur as the *O-phase*, which subsequently changes such as uneven tilting over to the *M-phase*, which likely nucleates at the surface. The dotted line is an approximate location of the interface.

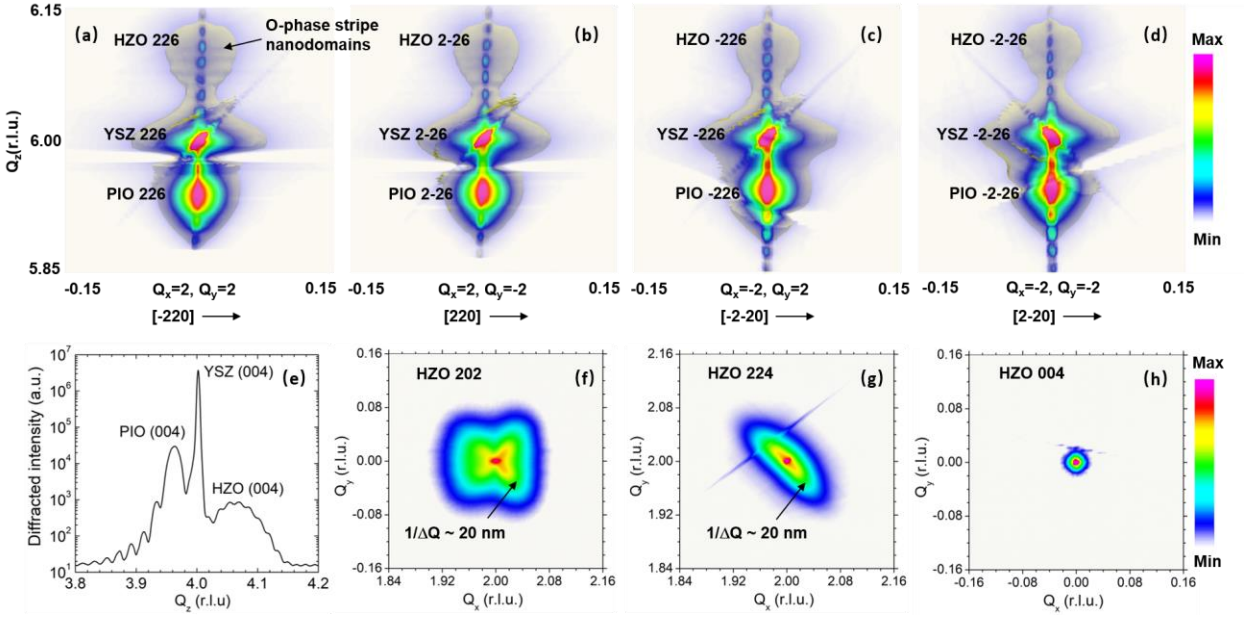

S4. Hard X-ray reciprocal space mapping and Bragg scan of the 15 nm sample.

(a)(b)(c)(d) are the 3D RSM images around the 226 $_{YSZ}$ peak for 15 nm HZO on 20 nm PIO. The multi-peaks of the o-phase indicate there are stripe nanodomains of o-phase in the 15 nm HZO film. **(e)** is the Bragg scan around the 004_{YSZ} peak. **(f)(g)(h)** are the 2D RSM images around the 202_{HZO} peak, the 224_{HZO} peak and the 004_{HZO} peaks respectively, showing the in-plane lattice information of HZO. The labeled nanodomains scattering (with periodicity of around 20nm) indicate o-phase domains with walls along in-plane [110] directions of the substrate.

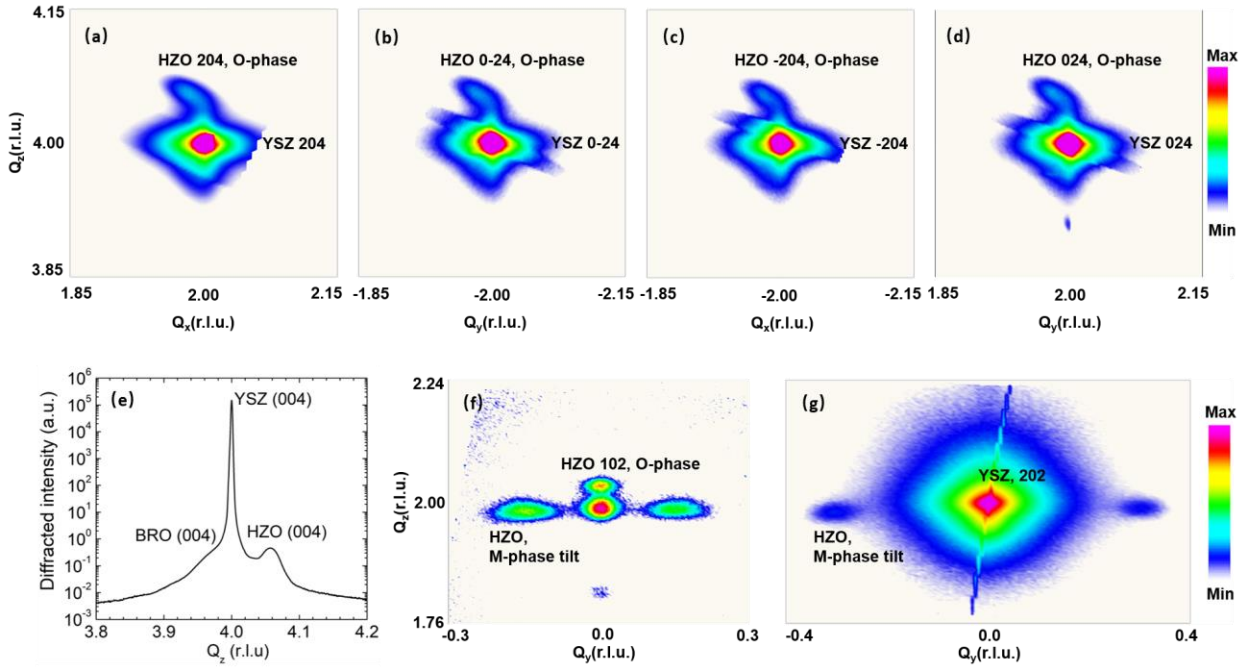

S5. Hard X-ray reciprocal space mapping and Bragg scan of the 40 nm sample.

(a)(b)(c)(d) are the 2D RSM images around the 204 $_{YSZ}$ peak for 40 nm HZO on 20 nm PIO. **(f)(g)** are 2D RSM around the 102_{HZO} and the 202_{YSZ} peaks respectively. Qx & Qy illustrate the in-plane lattice information, in the meantime, Qz shows the out-of-plane lattice information. The intensity of o-phase peak near the YSZ peak decreases compared with that in the 15 nm sample. In contrast, separated peaks of m-phase show up. **(e)** Bragg scan also indicates the quality degradation in thicker films.

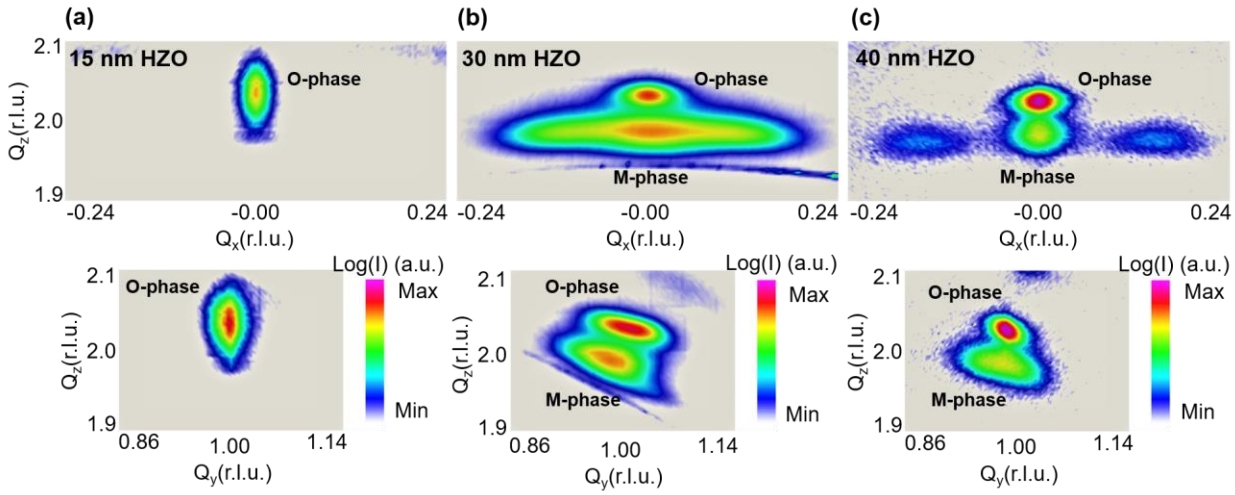

S6. Hard X-ray 2D reciprocal space mapping around the 012 $_{HZO}$ peak for 15, 30 and 40 nm samples

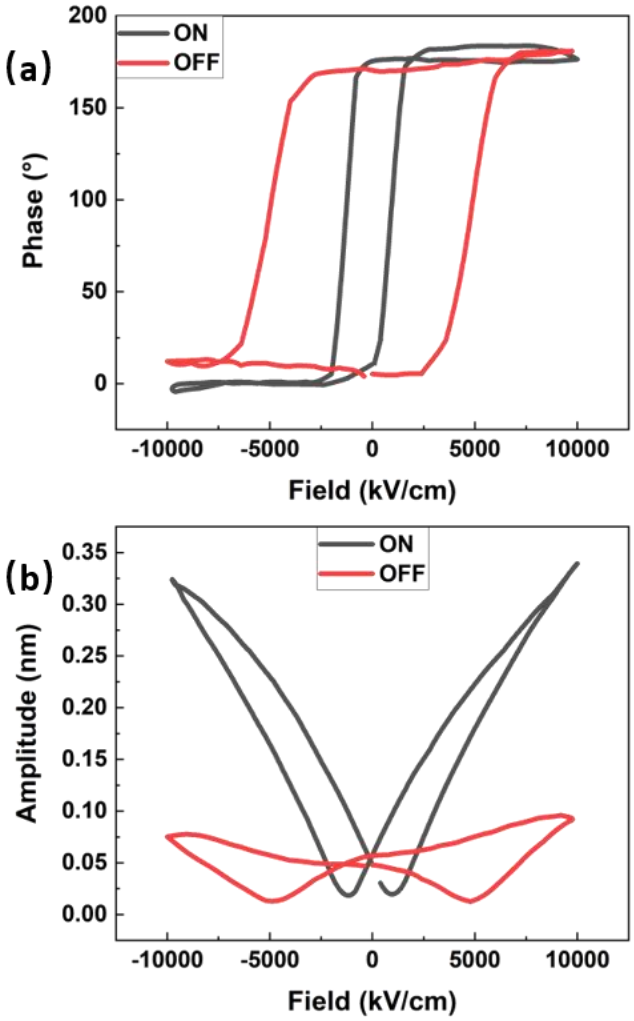

S7. Piezoresponse phase and amplitude loops for SRO/5nmHZO/PIO capacitors.

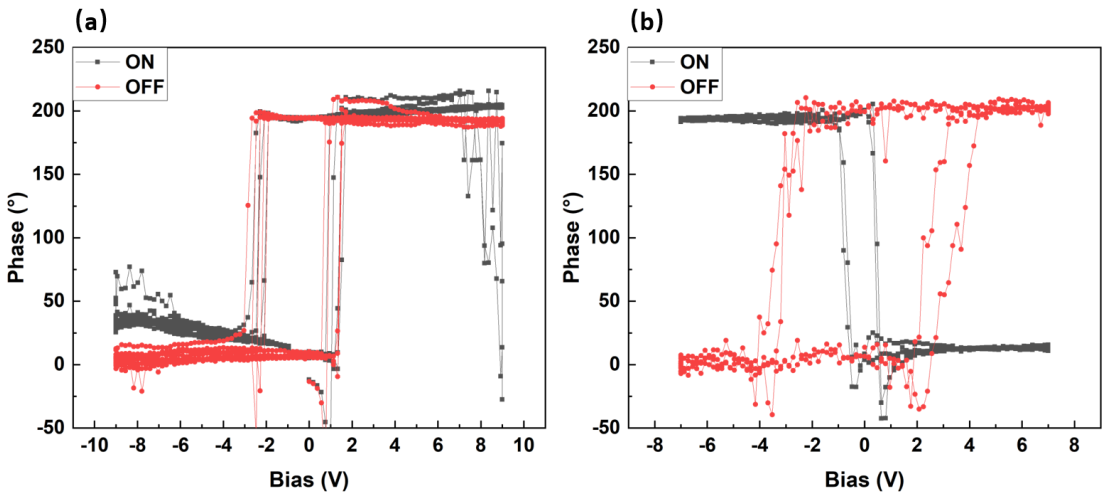

S8. Piezoresponse loops for SRO/BFO/SRO capacitors.

As a reference, we carried out the same set of piezoresponse measurements in both ON/OFF modes for $BiFeO_3$ (BFO) ferroelectric with $SrRuO_3$ top and bottom electrodes. **(a)** when BFO layer is 100-nm-thick; **(b)** when BFO layer is 6-nm-thick.

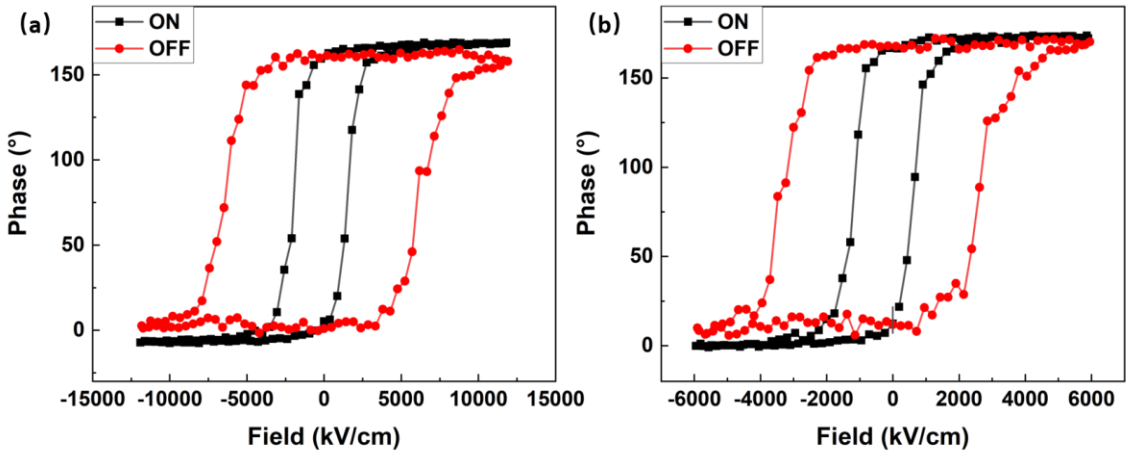

S9. Piezoresponse measurements for SRO/HZO/PIO samples at Asylum test facility.

We tested the same **(a)** 5 nm and **(b)** 10 nm samples as in **Figure 3d, e** at Asylum test facility and the ON/OFF difference is observed in these measurements as well.

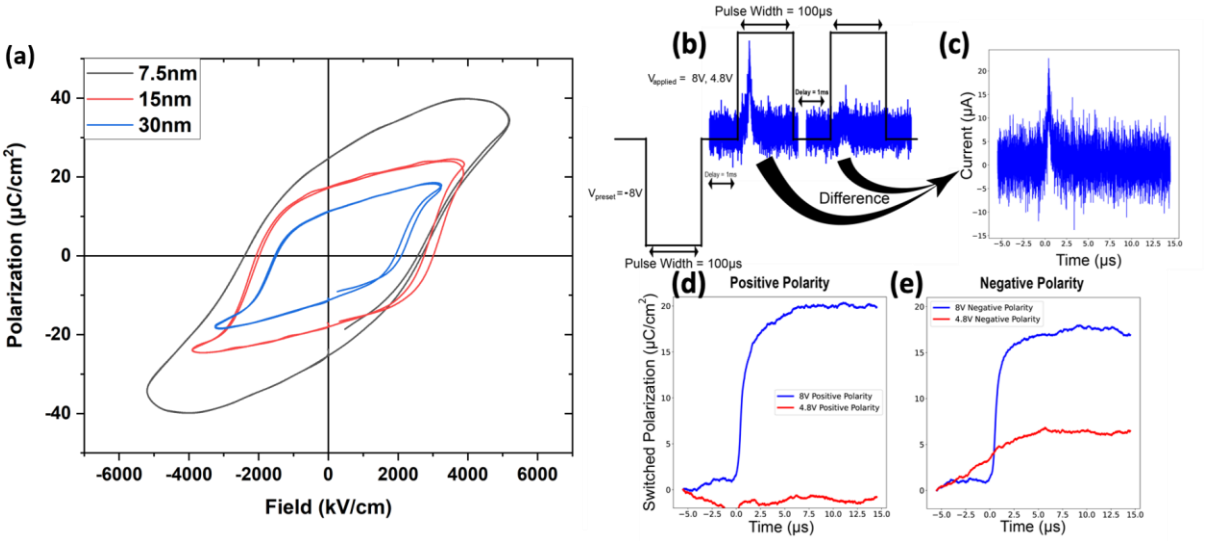

S10. Ferroelectric measurements on SRO/HZO/PIO capacitors.

(a) The polarization vs. field hysteresis loops measured at a test frequency of 100kHz on 30 nm SRO/ (7.5,15,30) nm HZO/ 20 nm PIO heterostructure capacitors with 12.5μm diameter;

(b) Test voltage profile (Black) and current response (Blue) measuring the polarization of the test capacitors;

(c) A typical switching current vs. time response, calculated as the difference in current response between the switching and non-switching pulses (first and second "up" pulses, respectively, in **(b)**);

(d) 30 nm SRO/ 30 nm HZO/ 20 nm PIO heterostructure capacitor switched polarization vs. time (integration of switching current) at 4.8V and 8V applied, measured in both positive and negative polarity;

(e) Switched polarization vs. time at 4.8V and 8V in the negative polarity. The polarity refers to the pulse sequence being applied to either the top or bottom electrode.

Calculation of the Gibbs free energy of m- and O-phases

The total free energy is the sum of the chemical energy (U-TS), the surface energy and the elastic strain energy. We set the Helmholtz free energy of the M-phase at 300K to 0, and the *O-phase* is 48 meV/f.u.[28]

(i) The elastic strain energy

In thin films, the source of stress is from the in-plane elastic strain that the substrate applies to the thin film layer, while the out-of-plane direction is free. For a film structure with orthogonal in-plane axis for all layers, we can only consider the three normal stresses σ_x, σ_y, σ_z, which can be calculated by:

$$\sigma_i = \frac{E}{(1-2\nu)(1+\nu)}[(1-\nu)\varepsilon_i + \nu(\varepsilon_j + \varepsilon_k)]$$

Where $\varepsilon_{i,j,k}$ is the lattice mismatch between the substrate and film layer in three directions, ν and *E* are Poisson's ratio and Young's modulus of the film material.

Here we set *z* direction as the out-of-plane direction, ε_x and ε_y are two in-plane mismatch ratios can be got directly from the lattice parameters. Because of $\sigma_z = 0$, we can get ε_z, then σ_x and σ_y. The ν and *E* value we used are from the materials project[31] The lattice parameter of the cubic YSZ substrate is 5.12 Å, while that of the HZO *m*- and *O-phase* are summarized as below from different computational and experimental results in literature for the hafnia/zirconia system.

Table S1. Lattice constants of HZO *m*- and *O-phase* from various sources

	a (Å)	b (Å)	c (Å)	Ref.
M-phase	5.11	5.18	5.28	[28]
	5.11	5.16	5.28	[28]
	4.95	5.06	5.08	[44]
	5.14	5.20	5.31	[45]
	5.12	5.19	5.28	[46]
	5.11	5.20	5.28	[28]
	5.09	5.20	5.24	[44]
	5.142	5.195	5.326	[31]
	5.234	5.268	5.418	[31]
O-phase	5.23	5.03	5.05	[28]
	5.22	5.04	5.05	[28]
	5.07	4.88	4.89	[44]
	5.29	5.01	5.08	[45]
	5.11	4.90	4.92	[46]
	5.24	5.04	5.05	[28]
	5.22	5.02	5.04	[44]
	5.269	5.04	5.074	[31]
	5.349	5.132	5.159	[31]

The elastic strain energy is then calculated as $\frac{1}{2}V \cdot \sum_i \sigma_i \varepsilon_i$.

(ii) The surface energy

The surface energy plays an important role in the total Gibbs free energy. Here we only count the interface of the HZO/top electrode or HZO/air in our thin film system. Thus, the surface energy per unit volume $\frac{A\gamma}{V} = \gamma/h$ is inverse proportional to the film thickness. We searched the reported surface energy for both *m*- and *O-phase*. We notice that in all the calculation results, the surface energy of *t*-phase and O-phase are very similar. Since the limited reported calculation result of the *O-phase* surface energy, we used some surface energy value of *t*-phase for the estimation of the *O-phase* surface energy.

Table S2. Surface energies of HZO m- and O-phase from various sources

	$\boldsymbol{\gamma}$ $(\mathbf{J}/\boldsymbol{m^2})$	**Ref.**		$\boldsymbol{\gamma}$ $(\mathbf{J}/\boldsymbol{m^2})$	**Ref.**
M-phase	3.2	[28]	**O-phase**	2.575	[28]
	3.4	[28]		3.15	[28]
	3.0	[28]		2.0	[28]
	3.7	[47]		1.03	[48]
	2.8	[47]		1.23	[48]
	3.45	[48]		2.1	[49]
	2.86	[48]			
	6.4	[49]			

Reference and Notes

[1] U. Schroeder, C. S. Hwang, H. Funakubo, *Ferroelectricity in doped hafnium oxide: materials, properties and devices*, Woodhead Publishing, 2019.

[2] P. Nukala, J. Antoja-Lleonart, Y. Wei, L. Yedra, B. Dkhil, B. Noheda, Acs Appl Electron Mater 2019, 1, 2585.

[3] Y. Wei, P. Nukala, M. Salverda, S. Matzen, H. J. Zhao, J. Momand, A. S. Everhardt, G. Agnus, G. R. Blake, P. Lecoeur, B. J. Kooi, J. Iniguez, B. Dkhil, B. Noheda, Nat Mater 2018, 17, 1095.

[4] S. Clima, S. R. C. McMitchell, K. Florent, L. Nyns, M. Popovici, N. Ronchi, L. D. Piazza, J. V. Houdt, G. Pourtois, "First-Principles Perspective on Poling Mechanisms and Ferroelectric/Antiferroelectric Behavior of Hf1-xZrxO2 for FEFET Applications", presented at *2018 IEEE International Electron Devices Meeting (IEDM)*, 1-5 Dec. 2018, 2018.

[5] T. S. Böscke, J. Müller, D. Bräuhaus, U. Schröder, U. Böttger, Applied Physics Letters 2011, 99, 102903.

[6] M. H. Park, H. J. Kim, Y. J. Kim, T. Moon, C. S. Hwang, Applied Physics Letters 2014, 104, 072901.

[7] M. H. Park, Y. H. Lee, H. J. Kim, Y. J. Kim, T. Moon, K. D. Kim, S. D. Hyun, T. Mikolajick, U. Schroeder, C. S. Hwang, Nanoscale 2017, 10, 716.

[8] T. Maeda, B. Magyari-Kope, Y. Nishi, "Identifying Ferroelectric Switching Pathways in HfO2: First Principles Calculations under Electric Fields", presented at *2017 IEEE International Memory Workshop (IMW)*, 14-17 May 2017, 2017.

[9] B. Johnson, J. L. Jones, Ferroelectr Doped Hafnium Oxide Mater Prop Devices 2019, 25.

[10] J. Lowther, J. Dewhurst, J. Leger, J. Haines, Physical review B 1999, 60, 14485.

[11] M. H. Park, T. Schenk, U. Schroeder, Ferroelectr Doped Hafnium Oxide Mater Prop Devices 2019, 49.

[12] E. D. Grimley, T. Schenk, T. Mikolajick, U. Schroeder, J. M. LeBeau, Advanced Materials Interfaces 2018, 5, 1701258.

[13] M. H. Park, T. Schenk, C. S. Hwang, U. Schroeder, Ferroelectr Doped Hafnium Oxide Mater Prop Devices 2019, 341.

[14] M. H. Park, Y. H. Lee, H. J. Kim, T. Schenk, W. Lee, K. D. Kim, F. P. G. Fengler, T. Mikolajick, U. Schroeder, C. S. Hwang, Nanoscale 2017, 9, 9973.

[15] T. Shimizu, K. Katayama, T. Kiguchi, A. Akama, T. J. Konno, O. Sakata, H. Funakubo, Sci Rep-uk 2016, 6, 32931.

[16] T. Shimizu, K. Katayama, T. Kiguchi, A. Akama, T. J. Konno, H. Funakubo, Applied Physics Letters 2015, 107, 032910.

[17] S. Migita, Y. Morita, W. Mizubayashi, H. Ota, "Preparation of epitaxial HfO2 film (EOT=0.5 nm) on Si substrate using atomic-layer deposition of amorphous film and rapid thermal crystallization (RTC) in an abrupt temperature gradient", presented at *2010 International Electron Devices Meeting*, 6-8 Dec. 2010, 2010.

[18] S. Migita, H. Ota, "(Invited) Epitaxial HfO", 2011.

[19] S. S. Cheema, D. Kwon, N. Shanker, R. d. Reis, S.-L. Hsu, J. Xiao, H. Zhang, R. Wagner, A. Datar, M. R. McCarter, C. R. Serrao, A. K. Yadav, G. Karbasian, C.-H. Hsu, A. J. Tan, L.-C. Wang, V. Thakare, X. Zhang, A. Mehta, E. Karapetrova, R. V. Chopdekar, P. Shafer, E. Arenholz, C. Hu, R. Proksch, R. Ramesh, J. Ciston, S. Salahuddin, Nature 2020, 580, 478.

[20] N. Tsuda, K. Nasu, A. Fujimori, K. Siratori, *Electronic Conduction in Oxides*, Springer Berlin Heidelberg, 2013.

[21] H. Sakai, H. Ohno, N. Oba, M. Kato, K. Yoshimura, Physica B: Condensed Matter 2003, 329-333, 1038.

[22] R. J. Bouchard, J. L. Gillson, Materials Research Bulletin 1971, 6, 669.

[23] K. Sardar, E. Petrucco, C. I. Hiley, J. D. B. Sharman, P. P. Wells, A. E. Russell, R. J. Kashtiban, J. Sloan, R. I. Walton, Angewandte Chemie International Edition 2014, 53, 10960.

[24] R. H. Wakabayashi, H. Paik, M. J. Murphy, D. G. Schlom, M. Brutzam, R. Uecker, R. B. van Dover, F. J. DiSalvo, H. D. Abruna, J. Electrochem. Soc. 2017, 164, H1154.

[25] R. Wang, A. Go, A. J. Millis, Physical Review B 2017, 95, 045133.

[26] A. Jaiswal, E. D. Wachsman, J. Electrochem. Soc. 2005, 152, A787.

[27] V. Esposito, B. H. Luong, E. Di Bartolomeo, E. D. Wachsman, E. Traversa, J. Electrochem. Soc. 2006, 153, A2232.

[28] R. Materlik, C. Künneth, A. Kersch, Journal of Applied Physics 2015, 117, 134109.

[29] M. H. Park, H. J. Kim, Y. J. Kim, W. Lee, T. Moon, C. S. Hwang, Applied Physics Letters 2013, 102, 242905.

[30] J. W. Matthews, A. E. Blakeslee, Journal of Crystal Growth 1974, 27, 118.

[31] K. Persson, Materials Project 2014.

[32] X. Sang, E. D. Grimley, T. Schenk, U. Schroeder, J. M. LeBeau, Applied Physics Letters 2015, 106, 162905.

[33] C. Ophus, Advanced Structural and Chemical Imaging 2017, 3, 13.

[34] A. Pryor, C. Ophus, J. Miao, Advanced Structural and Chemical Imaging 2017, 3, 15.

[35] R. Proksch, S. Kalinin, PFM App Note 2008.

[36] V. Janovec, Cechoslovackij fiziceskij zurnal 1958, 8, 3.

[37] H. F. Kay, J. W. Dunn, The Philosophical Magazine: A Journal of Theoretical Experimental and Applied Physics 1962, 7, 2027.

[38] S. J. Kim, D. Narayan, J.-G. Lee, J. Mohan, J. S. Lee, J. Lee, H. S. Kim, Y.-C. Byun, A. T. Lucero, C. D. Young, Applied Physics Letters 2017, 111, 242901.

[39] A. Gruverman, M. Alexe, D. Meier, Nature Communications 2019, 10, 1661.

[40] S. V. Kalinin, A. N. Morozovska, L. Q. Chen, B. J. Rodriguez, Reports on Progress in Physics 2010, 73, 056502.

[41] A. Gruverman, S. V. Kalinin, Journal of Materials Science 2006, 41, 107.

[42] D. J. Kim, J. Y. Jo, Y. S. Kim, Y. J. Chang, J. S. Lee, J.-G. Yoon, T. K. Song, T. W. Noh, Phys Rev Lett 2005, 95, 237602.

[43] R. R. Mehta, B. D. Silverman, J. T. Jacobs, Journal of Applied Physics 1973, 44, 3379.

[44] S. E. Reyes-Lillo, K. F. Garrity, K. M. Rabe, Physical Review B 2014, 90, 140103.

[45] T. D. Huan, V. Sharma, G. A. Rossetti, R. Ramprasad, Physical Review B 2014, 90, 064111.

[46] Q. Zeng, A. R. Oganov, A. O. Lyakhov, C. Xie, X. Zhang, J. Zhang, Q. Zhu, B. Wei, I. Grigorenko, L. Zhang, L. Cheng, Acta Crystallographica Section C 2014, 70, 76.

[47] W. Zhou, S. V. Ushakov, T. Wang, J. G. Ekerdt, A. A. Demkov, A. Navrotsky, Journal of Applied Physics 2010, 107, 123514.

[48] A. V. Radha, O. Bomati-Miguel, S. V. Ushakov, A. Navrotsky, P. Tartaj, Journal of the American Ceramic Society 2009, 92, 133.

[49] M. W. Pitcher, S. V. Ushakov, A. Navrotsky, B. F. Woodfield, G. Li, J. Boerio-Goates, B. M. Tissue, Journal of the American Ceramic Society 2005, 88, 160.

Acknowledgments
Z.Z., R.R., and D.G.S. acknowledge the support from ASCENT, one of six centers in JUMP, a Semiconductor Research Corporation (SRC) program sponsored by DARPA. H.P. acknowledges support from the National Science Foundation [Platform for the Accelerated Realization, Analysis, and Discovery of Interface Materials (PARADIM)] under Cooperative Agreement No. DMR-1539918. S.H. acknowledges support from the Quantum Materials program, funded by the U.S. Department of Energy, Office of Basic Energy Sciences, Materials Sciences Division. The electron microscopy work was carried out at the National Center for Electron Microscopy (Molecular Foundry@ LBNL). L.W.M. acknowledges the support of the National Science Foundation under grant DMR-1708615. V.A.S. acknowledge support from the U.S. Department of Energy Office of Science-Basic Energy Sciences, under Award Number DE-SC-0012375 for the development of the materials and synchrotron-based study of ferroic thin films. V.A.S. is grateful and would like to thank to Evguenia Karapetrova and Zhan Zhan for their support in performing the experiments at the Advanced Photon Source, Argonne National Laboratory. This research used resources of the Advanced Photon Source, a U.S. Department of Energy (DOE) Office of Science User Facility, operated for the DOE Office of Science by Argonne National Laboratory under Contract No. DE-AC02-06CH11357. Extraordinary facility operations were supported in part by the DOE Office of Science through the National Virtual Biotechnology Laboratory, a consortium of DOE national laboratories focused on the response to COVID-19, with funding provided by the Coronavirus CARES Act.